photonics

MDPI

Article

Multispectral Characterization of Additively Manufactured and Dip-Coated Axicons

Abhijeet Shrotri [1,*], Annamarija Starsaja [2,*], Suraj Joshi [2], Sascha Preu [2] and Oliver Stübbe [1]

[1] Technische Hochschule Ostwestfalen-Lippe, Institut für Energieforschung, Campusallee 12, 32657 Lemgo, Germany; oliver.stuebbe@th-owl.de

[2] Terahertz Devices and Systems, Technische Universität Darmstadt, Merckstraße 25, 64283 Darmstadt, Germany; suraj.joshi@tu-darmstadt.de (S.J.); sascha.preu@tu-darmstadt.de (S.P.)

* Correspondence: abhijeet.shrotri@th-owl.de (A.S.); annamarija.starsaja@tu-darmstadt.de (A.S.); Tel.: +49-5261-702-5449 (A.S.); +49-6151-16-28432 (A.S.)

Abstract

The use of additive manufacturing for rapid prototyping of near-infrared and terahertz components provides seamless and error-free production. This article discusses the additive manufacturing and post-processing of axicons and their performance evaluation using attenuation and near-field-measurements based fundamental techniques. The axicons are manufactured using the materials cyclic olefin copolymer (TOPAS) and polymethyl methacrylate (PMMA), for their respective use in terahertz and near-infrared applications. The optical and terahertz components manufactured using traditional 3D-printing processes, e.g., fused filament fabrication or stereolithography apparatus exhibit high surface roughness in the range of 15 ± 2.5 µm, resulting in undesired propagation and scattering in the near infrared wavelengths. This research work proposes an economical post-processing technique for additively manufactured terahertz and near-infrared axicons for applications in multispectral characterization, e.g., bio-sensing. The authors used an enhanced method of dip-coating, which involves interval dipping and intermittent hardening to achieve better surface finish. An emphasis is placed on interval dipping and intermittent hardening, which lead to excellent transparency in case of additively-manufactured near-infrared axicons. The dip-coated samples exhibit surface roughness below 10 nm. With the use of heated resin material as the coating layer, due to reduced viscosity, the resin material distributes uniformly over the surface of the 3D-printed terahertz and near-infrared axicons. The authors also observed that the DOF length deviation between unprocessed and enhanced dip-coated axicons remains within the measurement error estimation from analytical calculations. In addition to the improved surface finish and transparency, the coatings are also closely matched in refractive index to the axicon material. Such post-processed axicons pave the way for producing a wide array of systems in the fields of communication, imaging, and bio-sensing.

Keywords: additive manufacturing; stereolithography; dip-coating; post-processing

Check for updates

Received: 4 February 2026
Revised: 5 March 2026
Accepted: 6 March 2026
Published: 10 March 2026

Copyright: © 2026 by the authors. Licensee MDPI, Basel, Switzerland. This article is an open access article distributed under the terms and conditions of the Creative Commons Attribution (CC BY) license.

1. Introduction

Additive manufacturing (AM) of optical components is widely used for rapid prototyping and swift error correction [1,2]. Techniques such as stereolithography apparatus (SLA) and material jetting-based 3D-printing processes, e.g., inkjet 3D-printing using transparent materials, enable the fabrication of optical components such as lenses, plastic optical

fibers (POFs), and waveguides [3–6]. Implementation of photopolymerization-based manufacturing helps to develop complex geometrical structures, e.g., Fresnel lenses, Fresnel axicons, diffraction gratings [7,8], multi-material meta-surfaces and phase modulation elements [2,9]. Therefore, it is evident that when AM is combined with optical component prototyping, a cost-efficient alternative for current small batch manufacturing techniques can be derived [10]. However, the objects manufactured using polymer-based AM processes show high surface roughness on the order of few µm [11], i.e., in the range of one to a few wavelengths in the optical domain. The elimination of associated strong surface scattering of light requires post-processing. Simple hand polishing and lacquering-based approaches bring the surface roughness down to 5 µm, which is not sufficient for optical applications [12]. Additionally, state-of-the-art coating techniques based on high temperature processing are expensive and tedious [13,14]. Alternatives are lacquer spray coating or a completely automated complex industrial dip-coating procedure developed only for filament-based prototypes [15–17]. Such coating-based techniques can achieve nano-meter scale surface roughness [18,19]. However, very few techniques propose a simplified and cost-efficient approach for coating of lenses, e.g., our previous research [20].

Building upon current state-of-the-art designs of additively-manufactured axicons, reference [21] proposes a micro-axicon-based design for endoscopes. Notably, most of the applications of axicons appear in tomography and endoscopy, enabling improved imaging with large depth of focus (DOF) [22]. Similarly, reference [23] reports on 3D-printed axicons and phase plates composed of polypropylene (PP) and high density polyethylene (HDPE) for terahertz (THz) applications. Reference [24] summarizes detailed designs, parameter estimations, specific types of axicons, and their applications. Moreover, as discussed in reference [25], 3D-printed axicons of different apex angles for the THz spectral range are evaluated for the generation of arbitrary order Bessel beams. 3D-printed axicons with customized design have been experimentally demonstrated to enhance the signal focusing and robustness in short range THz communication links [26]. Motivated by these developments, the authors propose axicons for near-infrared (NIR) and THz applications. Such axicons can aid in the in- and outcoupling of THz waves [27] in waveguide-based biosensors and hold promise for their equivalent NIR counterparts.

This article extends our previous work from reference [27], where the authors investigated the AM and performance of THz axicons, with and without a dip-coating-based post-processing technique. In this work, we demonstrate low-loss additively manufactured and post-processed NIR axicons at 1550 nm. The authors discuss in detail the problems faced during design and rapid prototyping of the axicons, e.g., geometrical considerations due to layer-by-layer structures and post-processing related considerations, Additive manufacturing-based fabrication of axicons provides an alternative lucrative approach for production. Compared to the current state-of-the-art techniques, the method proposed by the authors in this research is advantageous for rapid prototyping and error correction for the manufacturing of complex geometries that are difficult to prototype using traditional manufacturing techniques, e.g., complex and non-standard aspheric, axicon and Fresnel lenses, etc. Moreover, in applications such as , endoscopy or bio-sensing, etc., the rapid error-evaluation-based approach helps in developing an optimal solution towards the finished product, e.g., manufacturing of non-standard waveguide designs implemented in bio-sensing as complex waveguides-based sensors. Additionally, an enhanced dip-coating based technique proposed by the authors is one of the most economical solutions for surface finishing compared to state-of-the-art post-processing techniques, e.g., polishing or diamond turning. Other advantages of dip-coating-based processing over traditional state-of-the-art post-processing techniques include the preservation of apex geometry, control of the surface roughness, surface damage protection and cost-effective scalability.

The outline of this article is as follows. Section 2 introduces axicons, briefly followed by the corresponding design parameters. Section 3 gives an overview of the manufacturing strategies and post-processing techniques. Section 4 extensively discusses the results for the additively manufactured THz and NIR axicons with an without post-processing. Section 5 summarizes the experimental evaluation, followed by the conclusion and outlook.

2. Theory and Design

Axicons have a conical front surface and rely on diffraction to obtain a long focal depth [28]. Unlike convex lenses that focus a parallel light beam around the focal point of the lens, the axicon produces an elongated focal depth profile called an interference line or depth of focus (DOF). This offers an advantage in applications where an elongated focal line is desired for imaging or spectroscopy. The applications of axicons include astronomy where parallel ring beams are generated. They are also utilized in the medical field for eye surgery and endoscopic imaging [24]. Moreover, the very basic use of axicons is in wave optics where Bessel beam generation is necessary. Axicons are usually manufactured using injection molding and preform-based heated molds, followed by polishing and milling. A separate milling of glass also produces axicons. Another interesting method for manufacturing axicons is diamond turning, which is used for high-precision axicon manufacturing without requiring any post-processing [29]. However, these processes are non-trivial and lack any rapid prototyping and error correction capabilities. Therefore, the authors concentrate on manufacturing axicons using additive-manufacturing-based processes, e.g., SLA [27].

For the defined range of the DOF of an axicon, the incident Gaussian beam guides itself into a second-order Bessel beam and forms concentric rings. Bessel beams show almost constant intensity distribution transverse to the direction of propagation. The beam properties within the range of DOF are nearly uniform, similar to a non-diffracting beam. It is, however only theoretically possible to generate perfect Bessel beams, and axicons can only produce nearly perfect Bessel beams [30]. To design axicons, a traditional approach based on apex angle calculations is utilized. The length of the DOF region is approximated using Equation (1), where R is the radius of the incident light beam, n is the refractive index of the axicon material, and β is the cone angle [31]. The cone angle is calculated using the predefined apex angle (α) of the axicon (please refer to Figure 1). The simplified formula given in Equation (1) approximates quite accurate results for smaller cone angles, but it is recommended to use the extended version for larger cone angle based calculations.

$$DOF = R \cdot \frac{\sqrt{1 - n^2 \sin^2 \beta}}{\sin \beta \cos \beta \left(n \cos \beta - \sqrt{1 - n^2 \sin^2 \beta} \right)} \approx \frac{R}{(n-1)\beta} \tag{1}$$

The second-order Bessel beam forms an interference ring behind the DOF region. The thickness of this ring (t) corresponds approximately to the radius of the incident light beam.

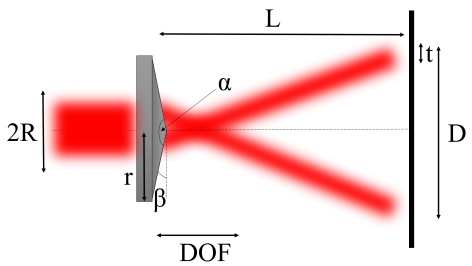


Figure 1. Pictorial representation of an axicon showing the Bessel beams after the DOF region.

The analytical calculation for the thickness of the interference ring is given by,

$$t = R \cdot \frac{\sqrt{1 - n^2 \sin^2 \beta}}{\cos \beta \left(n \sin^2 \beta + \cos \beta \sqrt{1 - n^2 \sin^2 \beta} \right)} \approx R \tag{2}$$

The ring diameter of the interference ring (d_r) is calculated using the simplified equation,

$$d_r = 2L \cdot \tan[(n-1)\beta] \tag{3}$$

There is a linear relationship between the ring diameter and the distance between the formed ring and the axicon. Another important parameter in the designing of axicons is the height of the axicon. The authors used Equation (4) to calculate the height of the axicon (h), where r is the radius of the axicon, and β is the cone angle:

$$h = r \cdot \tan \beta. \tag{4}$$

Based on a few reference measurements and $1/e^2$ method calculations in MATLAB R2024b, the authors approximate the NIR beam diameter as 10 mm. For the THz beam, the approximated beam diameter due to the placement of an aluminum foil-based circular aperture before the axicon does not exceed 20 mm for the investigated frequencies. Table 1 summarizes further design parameters for apex angles 140°, 150° and 160° that were calculated using MATLAB in order to design the axicons in Autodesk Fusion 360.

Table 1. Design parameters of NIR and THz axicons.

Apex Angle (α)	Cone Angle (β)	h	DOF (NIR)	DOF (THz)
140°	20°	5.46 mm	27.03 mm	54.05 mm
150°	15°	4.02 mm	36.04 mm	72.07 mm
160°	10°	2.65 mm	54.05 mm	108.11 mm

For the TOPAS material (for THz components) [12], the measured refractive index is 1.53, and for clear resin material (for NIR components), the refractive index at 1550 nm is 1.49. While designing the axicons, authors provided a thickness of 10 mm by designing and manufacturing an additional base structure to each axicon, in case post-processing requires better grip. These axicons also possess three stripes at 120°, each to be fitted inside the holders for further post-processing (explained in detail in Section 3). Figure 2 shows the exemplary 3D-representation and 2D-sketch of the axicon of apex angle 140°.

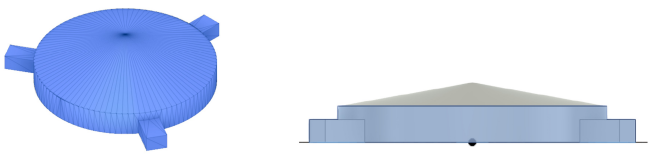


Figure 2. Autodesk Fusion 360 screenshot depicting the 3D-representation (**left**) and 2D-sketch (**right**) of an axicon with an apex angle of 140°.

3. Methodology

AM of optical components is a four-step process in which the 3D-CAD, standard triangulation language, or standard tessellation language (STL) file is initially sliced. This is followed by the prototype manufacturing with the help of layer-by-layer deposition. The component then undergoes post-processing to achieve the required transparency and attenuation. Our previous research from references [12,13] thoroughly discusses the

currently available materials and suitable processes for AM of NIR and THz components. The fabrication of THz-based waveguides and axicons usually utilizes TOPAS as the filament material, as it shows low absorption of the THz beam [12]. In the 3D-printer (Bambu Lab X1E) used for the manufacturing of THz axicons in our previous research [27], TOPAS filament deposition onto the build platform was carried out using the fused filament fabrication (FFF) process. The axicons were fabricated using an aligned rectilinear infill pattern and a layer-by-layer manufacturing process, with a layer thickness of 100 µm at an infill density of 100%.

As an extension to the work described in reference [20], this study utilizes a PMMA-based resin and SLA process for the manufacturing of NIR axicons. The newly fabricated NIR axicon shares the same design parameters as the THz axicon in reference [27], featuring a 140° apex angle. A Formlabs Form 3 SLA-based 3D-printer and Formlabs Clear resin V4 (PMMA-based resin) were used to manufacture the axicons. The fabrication process orients the axicons such that the flat surface contains the support structures for mechanical stability. These structures surround the surface to prevent the formation of in-process satellite drops and are removed later by mechanical breaking. The 3D-printer uses low force SLA, which facilitates support removal without affecting the surface finish. After printing, the structures were washed in isopropyl alcohol to remove any residual resin and were subsequently hardened under UV light. The bottom flat surface was polished using a wet-grinding machine, while the top surface remained unpolished to avoid structural deformation and potential parameter alterations. An improved and enhanced dip-coating process acts as the final post-processing step. This improved technique (termed hereafter as enhanced dip-coating) differs from the previous method (termed hereafter as simple dip-coating) reported in our research from reference [20], which contained the following steps:

1. Heating the PMMA-based resin to 70 °C, followed by immersing the optical components in heated resin for approximately 10 s.
2. A UV-hardening unit (Formlabs Form Cure) operating at a wavelength of 405 nm and with heating at 60 °C hardened the coated samples continuously for up to 30 min.

An initial Snell's law-based verification of the refractive index of the half cylindrical samples evaluated the effects of hardening and dip-coating on the refractive index of the resin [7]. The refractive index of the resin after washing remains the same as that of the liquid resin. After hardening, the refractive index of the material increases to 1.53. Additionally, a yellow hue and a few satellite drops were occasionally present in the post-processed samples. The yellow hue is caused by the thermal processes during the crosslinking of oligomers and monomers. These crosslinking reactions result in the formation of chromophores, which are responsible for the yellow hue [32,33]. The enhanced approach presented in this manuscript resolves these drawbacks by performing multiple dip-coating cycles (interval dipping) lasting more than 10 s, separated by 20–30 s intervals, to achieve a uniform coating layer followed by multiple hardening cycles performed at 60 °C in 5 min intervals (intermittent hardening). Gentle shaking after dip-coating removes excess resin and prevents its accumulation and subsequent formation of pendant drops at the lowest point of the sample, as observed in conventional dip-coating processes. The combination with intermittent hardening provides uniform crosslinking of the oligomers and monomers. Moreover, the authors observed a minor residual curvature with height variation of the order of ~1 µm over the lateral distance of 0.5 mm. Therefore, in case of the THz-wavelengths employed in this research, it is evident that such variation would not cause any influence on the transmission. Similarly for optical wavelengths, the surface modifications are minor and may not result in erroneous transmission.

Moreover,intermittent hardening prevents local overheating by limiting the crosslinking reactions and thereby the formation of chromophores. This suppresses the coloration

and satellite drop formation [34]. Figure 3 shows a step-by-step enhanced dip-coating approach based on interval dipping and intermittent hardening.

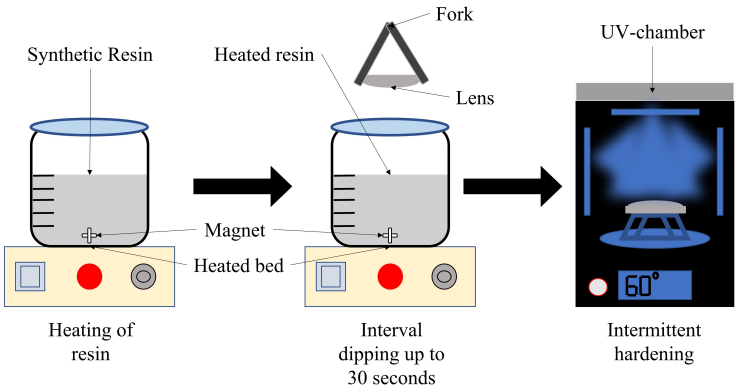


Figure 3. Step-by-step enhanced dip-coating approach based on interval dipping and intermittent hardening.

In the case of FFF of TOPAS, the intrinsic anisotropy and micro porosity cause a reduction in the refractive indices. The authors therefore used more than 100% (between 105% and 110% depending on the material humidity before starting the 3D-print) material flow to fill the gaps between the layers. The coating and axicon materials have matching refractive indices, and there is no index gradient present to worsen the functioning of the components. Furthermore, the authors also computed the relation between the dipping and hardening time based on the surface tension, thermal diffusivity and thickness of the object to be coated, and dipping thickness [35]. The relaxation time (T_r) equation from the Landau–Levich–Derjaguin Problem [36] of a viscous liquid, with η as the viscosity and L as the flow scale, is given by

$$T_r \approx \frac{\eta \times L^2}{\gamma}. \tag{5}$$

The derived dipping time T_d and hardening time T_h are given by

$$T_d \propto \sqrt{\frac{l}{\delta}}, \tag{6}$$

$$T_h \propto \frac{l^2}{\kappa}. \tag{7}$$

Here, l is the thickness of the lens, δ is the thickness of the coating layer, and κ is the thermal diffusivity.

4. Results and Discussion

A total of eight NIR-axicon samples were manufactured and characterized. Two samples were left unprocessed, while two samples each were post-processed by simple dip-coating, enhanced dip-coating, and polishing at the bottom surface. All samples were fabricated using identical design and 3D-printing parameters to ensure reproducibility and to validate the obtained results.

4.1. Surface Roughness and Transparency

Figure 4 depicts the achieved transparency after the enhanced dip-coating process for the THz and NIR axicon samples. The samples coated using the enhanced dip-coating are later mounted on holders 3D-printed using PLA in an FFF-based Prusa MK3S+ (Prusa research a.s., Prague, Czech Republic) 3D-printer. These holders are specially designed to fit inside the curing device so that the bottom surface of the 3D structures does not

touch the curing surface of the form cure avoiding the imprinting of dust or resin residue particles on the dip-coated surface. The authors concentrated only on post-processing using the Formlabs clear resin material to avoid refractive-index mismatch and probable Fabry Pérot effects. Research is currently being carried out with other suitable materials, e.g., Acrylonitrile Butadiene Styrene, Ormocore, and SU-8 as they show nearly similar refractive indices as the Formlabs Clear resin.

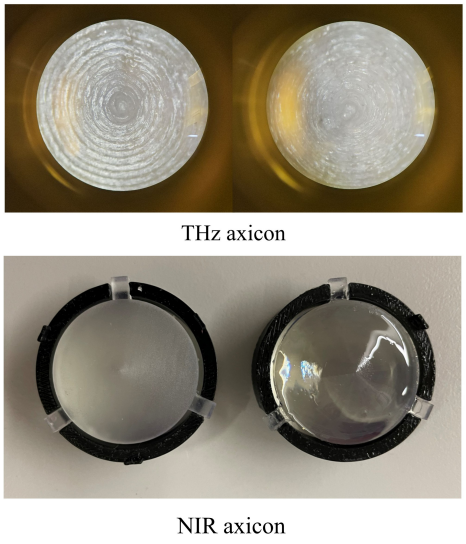


Figure 4. Achieved transparency of a THz-axicon (microscope image) (**top**) and a NIR-axicon (**bottom**) before and after enhanced dip-coating depicting the unprocessed (**left**) and enhanced dip-coated (**right**) axicon samples.

The enhanced approach shows that the combination of interval dipping and intermittent hardening offers an improved finish of the axicon surface. No visible accumulation of resin and thereby rounding of the apex of the axicon is observed. The combination of reduced viscosity and uniform crosslinking of oligomers and monomers followed by gentle shaking ensures a uniform thin coating layer over the axicon surface including the apex of the axicon. Moreover, the refractive index of the hardened layer and the axicon material stabilizes at 1.53 following the enhanced dip-coating process. This value represents an effective average over the coating thickness. Depth-resolved measurements are not performed, as the controlled curing using intermittent hardening ensures the uniform crosslinking of monomers and oligomers.

A profilometer (DEKTAK 6M from Bruker Corporation, Germany) measured the surface roughness of the NIR-axicon samples. The surface roughness R_a (arithmetic average of surface deviation) of the enhanced dip-coated sample is below 10 nm. The coating thickness of all 8 samples was between 10 µm and 14.5 µm. The boxplot in Figure 5 shows the corresponding mean and median surface thickness of the 8 measured samples. The observed results indicate good reproducibility of dip-coated surfaces. The surface roughness achieved using the simple dip-coating process and the enhanced dip-coating process is tabulated in Table 2. Corresponding measurement results are plotted in Appendix A.

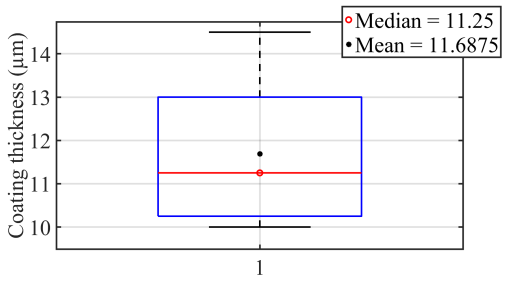


Figure 5. Boxplot depicting the mean and median values of the measured coating surface thickness of the 8 samples.

Table 2. Comparison of surface roughness after applying simple dip-coating and enhanced dip-coating-based post-processing.

Sample Type	Unprocessed	Simple Dip-Coating	Enhanced Dip-Coating
Roughness (R_a)	15 µm ± 2.5 µm	5 nm ± 2 nm	3 nm ± 2 nm

Next, the authors carried out a scattering loss-based transmission efficiency analysis using the aperture method [37] configuration with the aperture-controlled detector field of view. The aperture-controlled detector measures the non-scattered component of transmission, excluding the scattered light (specular transmission efficiency) in the first step, and then the total transmission efficiency. Later, the scattering loss was estimated using the difference between the specular and total efficiency. The proportional relation between scattering loss (S) and surface roughness is given as

$$S \propto \left(\frac{4\pi\sigma}{\lambda}\right). \tag{8}$$

where σ is the surface roughness, and λ is the wavelength [38].

At THz frequencies, the surface roughness of unprocessed TOPAS axicons corresponds to the scatter fraction of 1–2%. This results in very minor scattering losses. On the other hand, for NIR wavelengths (in this case 1550 nm), the same surface roughness yields nearly 30–40% power loss compared to the enhanced dip-coated axicon. Using the aperture method, the authors observed that the enhanced dip-coated sample maintains high transmission with only 3% scatter fraction, whereas the unprocessed sample exhibits significantly reduced efficiency with a scatter fraction of 30%, in very good agreement with theoretical calculations. Figure 6 depicts the corresponding bar plot of the transmission efficiency for both unprocessed and enhanced dip-coated samples.

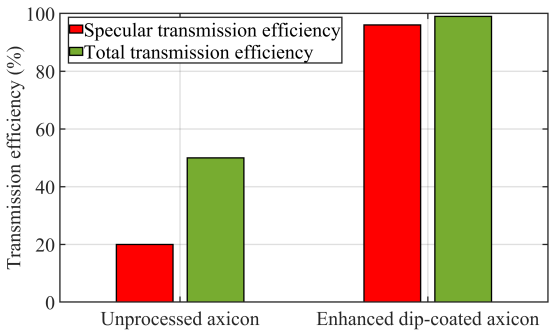


Figure 6. Bar plot depicting the transmission efficiency for (**left**) unprocessed and (**right**) enhanced dip-coated NIR axicons.

4.2. Terahertz Characterization of TOPAS-Based Axicons

The authors initially carried out the beam profile measurement of TOPAS THz axicons. Reference [27] details the experimental setup for this measurement. The distances between the axicon and THz detector are chosen to be 55 mm and 82 mm, which correspond to regions in the vicinity of or within the DOF of the axicon for the frequencies in the range of 100–300 GHz. Figure 7 illustrates the normalized electric-field-intensity distribution of unprocessed and dip-coated THz axicons manufactured using TOPAS and the FFF process. The measured median DOF length of unprocessed and enhanced dip-coated THz-axicons of apex angle 140° is approximated to 56.66 mm and 55.33 mm with a relative statistical deviation of 4%. The deviation is within the measurement error, as the film thickness remains a small fraction of the THz wavelength (here: λ = 1–3 mm).

Moreover, the TOPAS-based THz axicons feature a slight refractive-index-mismatch between coating material (Formlabs Clear Resin V4, refractive index: 1.5143) and the base material (TOPAS, refractive index: 1.5251), causing a very minor reflection on the order of 4.4×10^{-5}. However, the resulting Fabry-Pérot oscillations remain below the measurement error in most cases and do not impede the alignment process. By using the same dipping solvent described in Section 3 for post-processing, even this minor reflection could be mitigated.

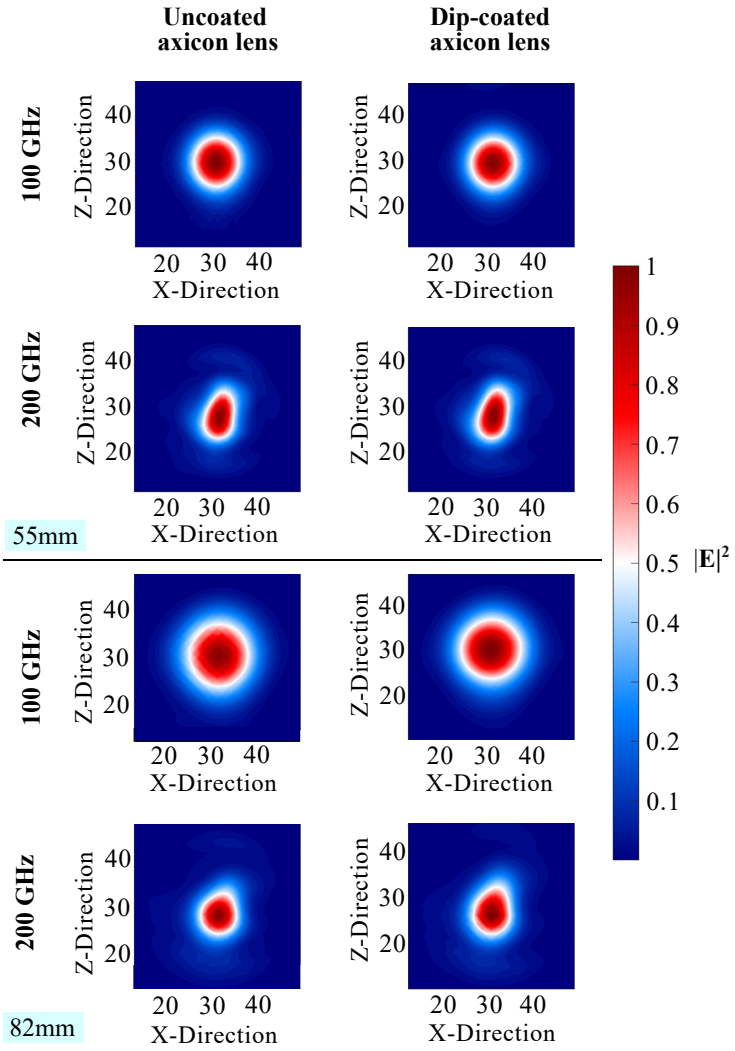


Figure 7. Normalized electric-field-intensity distribution of the unprocessed (**left**) and dip-coated (**right**) THz TOPAS-based axicons in the frequency range of 100–200 GHz at distances 55 mm and 82 mm from the receiver [27].

4.3. Near-Infrared Characterization of PMMA-Based Axicons

Figure 8 illustrates the experimental setup for the PMMA-based NIR axicon evaluation. The setup includes a Thorlabs MCLS1 fiber-coupled laser module that provides four selectable wavelengths (635 nm, 850 nm, 1310 nm, and 1550 nm). For the analysis of NIR axicons, the 1550 nm output was selected, delivering 1.2 mW of optical power. The laser beam exits the multimode FC/PC fiber patch cable (with 50 µm core diameter) into free space, where a conventional convex lens (C-L) is used to align the setup and form a quasi-parallel transmission beam. The Anritsu ML9001A power meter from Anritsu Corporation with a 1550 nm detector module is placed on an automated XYZ stage, operated by a Newport MM4006 motion controller from Newport Corporation.

The detector and power-meter readings determine the approximate beam diameter at the incident plane of the additively manufactured axicon lens (AX-L). The AX-L features a diameter of 30 mm, ensuring that the optical beam remains non-truncated. A reference measurement without the axicon provides a baseline for subsequent analysis. The beam profile of a 1550 nm beam transmitted through an axicon with an apex angle of 140° was first calculated and later compared with the measured and processed experimental results (see Figure 9, dashed plot). Initially, the distance set between the detector module and the calculated DOF is 5 mm. Unprocessed and post-processed (polished at the bottom surface, dip-coated and enhanced dip-coated) axicons are then placed between the convex lens and the detector one after another to analyze the DOF of the axicon. The detector scans the axicon's calculated DOF region in 2 mm steps. The results demonstrate that the dip-coated axicon focuses the beam within the DOF region, whereas the unprocessed axicon fails to achieve this.

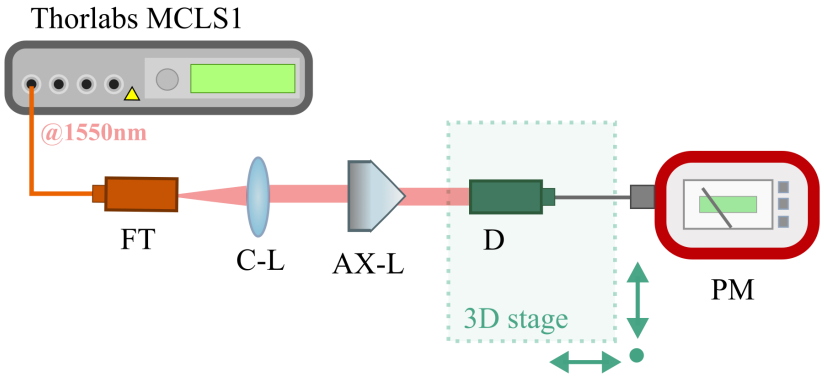


Figure 8. Experimental setup for the measurement of the beam profile of NIR PMMA-based axicons at 1550 nm.

As the detector uses an aperture with a diameter of 9.5 mm, the data are integrated and normalized to the detector area and an image-processing-based evaluation is used to correctly represent the measured results. The authors used the following image processing tools (described here step-by-step) to generate the final comparison of the DOF results:

1. Digitization: The continuous image is scanned at fixed raster positions. The underlying grid is determined by the sensor architecture [39].
2. Interpolation: Interpolation is used to obtain the continuous signal from the digitized and discrete scan.
3. Deconvolution: At the end of image processing, deconvolution using a point spread function is utilized. This is the final image reconstruction step using inverse filtering

and Wiener deconvolution. A mathematical representation explaining a measured image b, point spread function c, and original image X is given by

$$b = c \times X + \eta, \tag{9}$$

where η is the additive noise independent of the signal. The measured image acts as a low pass filter attenuating high frequency image details. It is observed that the Wiener deconvolution is a robust method of decompressing that delivers consistent results using the measurement data.

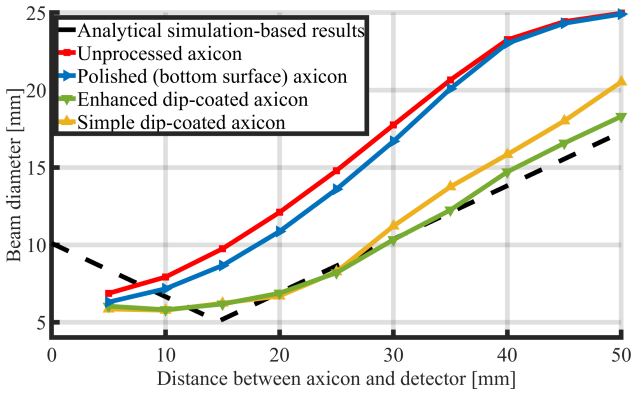


Figure 9. Beam profile of NIR PMMA-based axicons with an apex angle of 140°.

Finally, the raw and processed data sets are compared to verify the DOF of the NIR axicons. Figure 9 shows an exemplary result depicting the processed plots for the beam profile of the axicons (unprocessed, polished at bottom surface, simple dip-coated and enhanced dip-coated) with an apex angle of 140°. It can be concluded from these results that the beam profile of the enhanced dip-coated axicon and simple dip-coated axicon matches the analytical results derived from the design parameters. Figure 10 shows the total integrated power for the enhanced dip-coated axicons and simple dip-coated axicons for varying detector positions. The output power measurements indicate that the strongest power concentration occurs within the half of the DOF region, located between 13 mm and 17 mm. This region aligns well with the original design parameters indicating the beginning of the DOF region. The total integrated power starts dropping after the distance of 33 mm, followed by the formation of an interference ring, which results in second-order Bessel beams at 60 mm for the considered axicon. The enhanced dip-coated axicon shows less attenuation of the beam as compared to simple dip-coated samples, due to uniform coating and reduced satellite drops. The high absorption in the unprocessed axicons prevents any clear or reliable conclusions regarding the DOF and the beam profile. From these results, it is evident that the enhanced dip-coating process with interval dipping and intermittent hardening, provides higher transparency, better finishing in terms of surface roughness, reduced attenuation, and marginal effects on the targeted refraction.

The reduced surface roughness also promises better wave propagation with minimal scattering. Finally, two NIR PMMA-based axicon samples of apex angles 150° and 160° were additively manufactured and post-processed using the enhanced dip-coating process. A comparatively similar behavior is observed for the same, reinforcing the critical role of the dip-coating based post-processing. The comparison of the beam profiles for measured enhanced dip-coated axicon samples with analytical calculations for axicons of apex angles 150° and 160° is shown in Figure 11.

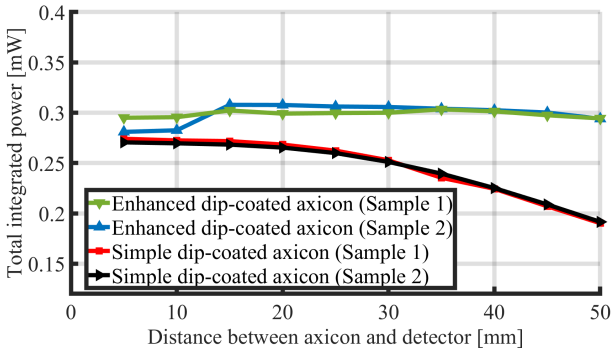


Figure 10. Integrated optical power at different distances to estimate the DOF region of NIR PMMA-based axicons with an apex angle of 140°.

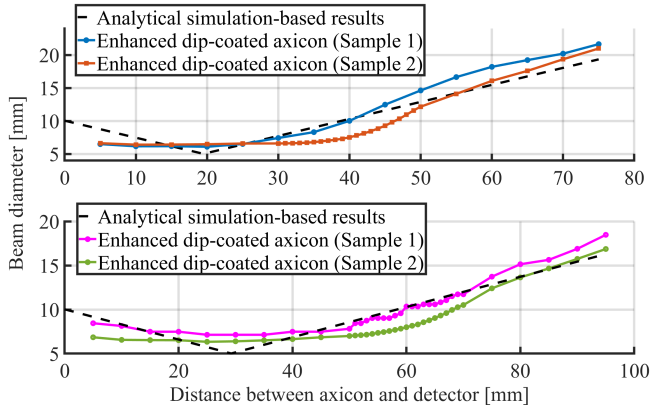


Figure 11. Beam profile of NIR PMMA-based axicons with an apex angle of 150° (**top**) and 160° (**bottom**).

4.4. Discussion

The experimental results demonstrate that the enhanced dip-coating based on interval dipping and intermittent hardening significantly improves the optical quality of the additively manufactured axicons. The intermittent hardening mitigates the risk of localized heating and cross-linking reactions linked to the formation of chromophores. This leads to better transparency and surface finish compared to the unprocessed samples. Similar coating techniques are already implemented as state-of-the-art post-processing methods; however, these approaches rely on continuous hardening that leads to non-uniform polymerization and yellow hue causing increased optical losses. The surface roughness characterization proves that the enhanced dip-coating provides significantly lower surface roughness (below 10 nm) than the unprocessed sample (15 µm ± 2.5 µm). The reduced surface roughness minimizes scattering defined by the Rayleigh–Rice theory, which plays a pivotal role in NIR optics. The optical quality surface finish is achieved without aggressive mechanical finishing, demonstrating a practical and scalable alternative for complex geometries. The surface shape and geometry remain close to that of the uncoated lenses and the designed shape, without any noteworthy discrepancies in DOF. This was verified using measured beam profiles for axicons of apex angles 140°, 150° and 160°. The measurements show median DOF lengths of 56.66 µm for unprocessed THz-axicons and 55.33 µm for enhanced dip-coated THz-axicons. Similarly, the median DOF length for unprocessed NIR-axicon is approximated to 28.75 mm, and for enhanced dip-coated NIR-axicons to 28.25 mm. Therefore, any DOF deviations between the enhanced dip-coated and unprocessed axicons remain within the measurement error from the analytical calculations of beam profiles. To the best of the authors' knowledge, this research proposes one of the first systematic investigations of interval dipping combined with intermittent

hardening to post-process additively manufactured components operating in the NIR and THz spectral regions.

5. Conclusions and Outlook

This work demonstrates an interval dipping- and intermittent hardening-based enhanced dip-coating process for generating optically smooth surfaces of additively manufactured axicons operating in the NIR and THz regime. By interrupting the hardening cycles, the process mitigates localized heating and results in uniform polymerization.

The developed post-processing method enables a surface roughness of the additively manufactured components below 10 nm, while preserving the designed geometry and beam profile of the components. The close refractive index matching between the coating layer and substrate ensures efficient transmission and no Fabry Pérot effects.

For FFF-based TOPAS axicons and SLA-based PMMA axicons, this method establishes a scalable post-processing approach and provides an alternative for the manufacturing of cutomizable and complex axicon geometries.

The improved surface finish and optical transmission ensure the use of additively manufactured and enhanced dip-coated axicons in advanced applications, e.g., bio-sensing, endoscopy, etc. Future work will extend the range of materials and explore ultra-precise thin-film deposition and hybrid coating to further tailor the functional integration.

Author Contributions: Conceptualization, A.S. (Abhijeet Shrotri), A.S. (Annamarija Starsaja) and S.J.; methodology, A.S. (Abhijeet Shrotri); validation, A.S. (Abhijeet Shrotri); measurements and formal analysis, A.S. (Abhijeet Shrotri), A.S. (Annamarija Starsaja) and S.J.; investigation, A.S. (Abhijeet Shrotri); resources, A.S. (Abhijeet Shrotri), S.J. and A.S. (Annamarija Starsaja); writing—original draft preparation, A.S. (Abhijeet Shrotri); writing—review and editing, A.S. (Abhijeet Shrotri), A.S. (Annamarija Starsaja), S.J., S.P. and O.S.; supervision, S.P. and O.S.; project administration, A.S. (Abhijeet Shrotri), S.P. and O.S.; funding acquisition, S.P. and O.S. All authors have read and agreed to the published version of the manuscript.

Funding: This research was funded by Deutsche Forschungsgemeinschaft (German Research Foundation) grant number 502254396, and the APC was funded by the Open Access Funds of Technische Hochschule Ostwestfalen-Lippe.

Data Availability Statement: Data underlying the results presented in this paper are not publicly available at this time, but they may be obtained from the authors upon reasonable request.

Acknowledgments: We thank Tobias Christophliemke and Silke Schober for laboratory support and device management and Lea Vogel for experimental evaluation.

Conflicts of Interest: The authors declare no conflicts of interest.

Appendix A. Supporting Data

The authors manufactured cube samples of volume 1 cm^3 to evaluate the surface roughness of the unprocessed and enhanced dip-coated objects. Figure A1 depicts the corresponding evaluation of surface roughness measurements for an enhanced dip-coated sample and an unprocessed sample using a DEKTAK 6M profilometer from Bruker Corporation (Billerica, MA, USA). The raw surface profiles measured by the system exhibit a pronounced low-order curvature despite the samples being nominally flat. This curvature does not represent surface roughness but arises from a combination of instrumental effects. To isolate the true roughness, the low-order form was removed by polynomial detrending, followed by spatial filtering to suppress long-wavelength waviness, yielding a band-limited surface profile. Roughness parameters, especially the arithmetic mean surface height R_a, are calculated from these form-removed profiles. The resulting plots therefore highlight only the micro-scale surface variations, enabling an accurate comparison

of surface roughness between the samples. The authors observed the surface roughness for multiple unprocessed and enhanced dip-coated samples and confirmed that the surface roughness of the enhanced dip-coated samples lies in the range of sub 10 nm, with a minimum calculated surface roughness of 3.23 nm.

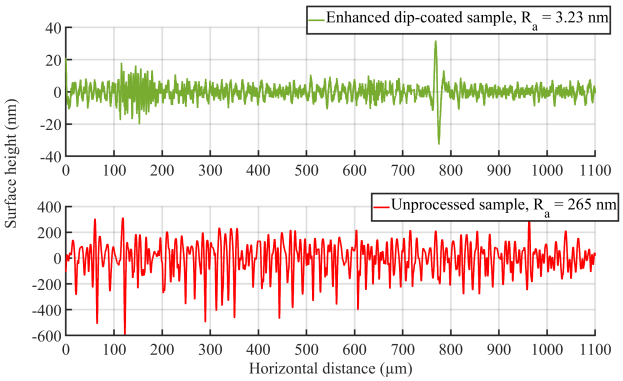


Figure A1. Evaluation of surface roughness measurements (R_a) of enhanced dip-coated (**top**) and unprocessed samples (**bottom**) with optimal 3D-print quality reference.

References

1. Thompson, M.K.; Moroni, G.; Vaneker, T.; Fadel, G.; Campbell, R.I.; Gibson, I.; Bernard, A.; Schulz, J.; Graf, P.; Ahuja, B.; et al. Design for Additive Manufacturing: Trends, opportunities, considerations, and constraints. *CIRP Ann.* **2016**, *65*, 737–760. [CrossRef]
2. Berglund, G.; Wisniowiecki, A.; Gawedzinski, J.; Applegate, B.; Tkaczyk, T.S. Additive manufacturing for the development of optical/photonic systems and components. *Optica* **2022**, *9*, 623–638. [CrossRef]
3. Shan, Y.; Hua, J.; Mao, H. 3D Printing of Optical Lenses Assisted by Precision Spin Coating. *Adv. Funct. Mater.* **2024**, *34*, 2407165. [CrossRef]
4. Heinrich, A.; Rank, M. *3D Printing of Optics*; SPIE: Bellingham, WA, USA, 2018.
5. Trunin, P.; Cafiso, D.; Beccai, L. Design and 3D printing of soft optical waveguides towards monolithic perceptive systems. *Addit. Manuf.* **2025**, *100*, 104687. [CrossRef]
6. Elkaseer, A.; Chen, K.J.; Janhsen, J.C.; Refle, O.; Hagenmeyer, V.; Scholz, S.G. Material jetting for advanced applications: A state-of-the-art review, gaps and future directions. *Addit. Manuf.* **2022**, *60*, 103270. [CrossRef]
7. Shrotri, A.; Beyer, M.; Stübbe, O. Manufacturing and analyzing of cost-efficient fresnel lenses using stereolithography. In *Proceedings of the 3D Printed Optics and Additive Photonic Manufacturing II. International Society for Optics and Photonics*; SPIE: Bellingham, WA, USA, 2020; Volume 11349, p. 113490N. [CrossRef]
8. Hua, J.; Shan, Y.; Wu, S.; Mao, H. Three-Dimensional Printed Diffraction Gratings Drop Coated by Different Resins and Their Mechanism. *J. Manuf. Sci. Eng.* **2023**, *146*, 011001. [CrossRef]
9. Zhu, J.; Yang, Y.; Hu, N.; Liao, S.; Nulman, J. Additively Manufactured Multi-Material Ultrathin Metasurfaces for Broadband Circular Polarization Decoupled Beams and Orbital Angular Momentum Generation. *ACS Appl. Mater. Interfaces* **2021**, *13*, 59460–59470. [CrossRef] [PubMed]
10. Klenam, D.; McBagonluri, F.; Asumadu, T.; Osafo, S.; Bodunrin, M.; Agyepong, L.; Osei, E.; Mornah, D.; Soboyejo, W. Additive manufacturing: Shaping the future of the manufacturing industry—Overview of trends, challenges and opportunities. *Appl. Eng. Sci.* **2025**, *22*, 100224. [CrossRef]
11. Golhin, A.P.; Tonello, R.; Frisvad, J.R.; Grammatikos, S.; Strandlie, A. Surface roughness of as-printed polymers: A comprehensive review. *Int. J. Adv. Manuf. Technol.* **2023**, *127*, 987–1043. [CrossRef]
12. Shrotri, A.; Mukherjee, A.K.; Lohöfener, S.; Springer, A.; Stübbe, O.; Preu, S. Additive manufacturing and characterization of hollow core metal and topas waveguides for Terahertz sensor systems. In Proceedings of the 2023 48th International Conference on Infrared, Millimeter, and Terahertz Waves (IRMMW-THz), Montreal, QC, Canada, 17–22 September 2023; pp. 1–2. [CrossRef]
13. Beyer, M.; Shrotri, A.; Stübbe, O. Evaluation of stereolithography processes for the production of lens prototypes. In Proceedings of the Production Engineering and Management, Trieste, Italy, 3–4 October 2019; TH OWL: Lemgo, Germany, 2019; Volume 11349, pp. 227–239.
14. Žigon, J.; Karič, M.; Pavlič, M. Surface Finishing of 3D-Printed Polymers with Selected Coatings. *Polymers* **2020**, *12*, 2797. [CrossRef] [PubMed]

15. Sarkar, A.K.; Sarmah, D.; Baruah, S.; Datta, P. An Optimized Dip Coating Approach for Metallic, Dielectric, and Semiconducting Nanomaterial-Based Optical Thin Film Fabrication. *Coatings* **2023**, *13*, 1391. [CrossRef]
16. Rauh, F.; Bienek, O.; Sharp, I.D.; Stutzmann, M. Conversion of a 3D printer for versatile automation of dip coating processes. *Rev. Sci. Instrum.* **2023**, *94*, 083901. [CrossRef]
17. Trinh, T.; Smihi, M.; Koev, L.; Zielinski, R. Dip Coating Process for Optical Elements. U.S. Patent US20040096577A1, 20 May 2004.
18. Vaidya, N.; Solgaard, O. 3D printed optics with nanometer scale surface roughness. *Microsyst. Nanoeng.* **2018**, *4*, 18. [CrossRef] [PubMed]
19. Evertz, A.; Schrein, D.; Olsen, E.; Hoffmann, G.A.; Overmeyer, L. Dip coating of thin polymer optical fibers. *Opt. Fiber Technol.* **2021**, *66*, 102638. [CrossRef]
20. Shrotri, A.; Preu, S.; Stübbe, O. Achieving Transparency and Minimizing Losses of Rough Additively Manufactured Optical Components by a Dip-Coating Surface Finish. *Coatings* **2025**, *15*, 210. [CrossRef]
21. Ruchka, P.; Kushwaha, A.; Marathe, J.A.; Xiang, L.; Chen, R.; Kirk, R.W.; Tan, J.T.M.; Bursill, C.; Verjans, J.; Thiele, S.; et al. 3D-printed micro-axicon enables extended depth-of-focus intravascular optical coherence tomography in vivo. *Adv. Photonics* **2025**, *7*, 026003. [CrossRef]
22. Kumar, P.; Martin, H.; Henning, A.; Jiang, J. Probing depth enhancements of spectral domain optical coherence tomography using axicons for the inspection of additively manufactured polymer parts. In Proceedings of the Joint Special Interest Group Meeting Between Euspen and ASPE, Leuven, Belgium, 19–21 September 2023.
23. Ahmed, M. 3D Printed Optical Components for THz-Spectroscopy. Master Thesis, Johannes Kepler University Linz, Linz, Austria, March 2019.
24. Khonina, S.N.; Kazanskiy, N.L.; Khorin, P.A.; Butt, M.A. Modern Types of Axicons: New Functions and Applications. *Sensors* **2021**, *21*, 6690. [CrossRef]
25. Wei, X.; Liu, C.; Niu, L.; Zhang, Z.; Wang, K.; Yang, Z.; Liu, J. Generation of arbitrary order Bessel beams via 3D printed axicons at the terahertz frequency range. *Appl. Opt.* **2015**, *54*, 10641–10649. [CrossRef]
26. Bodet, D.; Petrov, V.; Petrushkevich, S.; Jornet, J.M. Sub-terahertz near field channel measurements and analysis with beamforming and Bessel beams. *Sci. Rep.* **2024**, *14*, 19675. [CrossRef]
27. Shrotri, A.; Joshi, S.; Vogel, L.; Starsaja, A.; Stübbe, O.; Preu, S. Terahertz Axicon Lenses. In Proceedings of the 2025 50th International Conference on Infrared, Millimeter, and Terahertz Waves (IRMMW-THz), Helsinki, Finland, 17–22 August 2025; pp. 1–2. [CrossRef]
28. Shi, L.; Dong, X.; Deng, Q.; Lu, Y.; Ye, Y.; Du, C. Design and characterization of an axicon structured lens. *Opt. Eng.* **2011**, *50*, 063001. [CrossRef]
29. Bachus, K.; de Lima Filho, E.S.; Wlodarczyk, K.; Oleschuk, R.; Messaddeq, Y.; Loock, H.P. Fabrication of axicon microlenses on capillaries and microstructured fibers by wet etching. *Opt. Express* **2016**, *24*, 20346–20358. [CrossRef] [PubMed]
30. Jaroszewicz, Z. *Axicons: Design and Propagation Properties*; Research and Development Treatises; Polish Chapter of SPIE: Warsaw, Poland, 1997.
31. González-Acuña, R.G.; Chaparro-Romo, H.A.; Gutiérrez-Vega, J.C. *Analytical Lens Design*; IOP Publishing: Bristol, UK, 2020; pp. 2053–2563. [CrossRef]
32. Allen, N.S.; Edge, M.; Hussain, S. Perspectives on yellowing in the degradation of polymer materials: inter-relationship of structure, mechanisms and modes of stabilisation. *Polym. Degrad. Stab.* **2022**, *201*, 109977. [CrossRef]
33. Krauklis, A.E.; Echtermeyer, A.T. Mechanism of Yellowing: Carbonyl Formation during Hygrothermal Aging in a Common Amine Epoxy. *Polymers* **2018**, *10*, 1017. [CrossRef] [PubMed]
34. Lim, J.H.; Shin, S.H.; Jung, Y.E.; An, H.; Kim, J.E. Influence of heat-assisted vat photopolymerization on the physical and mechanical characteristics of dental 3D printing resins. *Sci. Rep.* **2025**, *15*, 1710. [CrossRef] [PubMed]
35. Levich, B.; Landau, L. Dragging of a liquid by a moving plate. *Acta Physicochim. U.R.S.S.* **1942**, *XVII*, 42–54.
36. Maleki, M.; Reyssat, M.; Restagno, F.; Quéré, D.; Clanet, C. Landau–Levich menisci. *J. Colloid Interface Sci.* **2011**, *354*, 359–363. [CrossRef]
37. Chen, G.; Zhang, T.; Lu, R. Aperture design to improve the sensitivity of detecting subsurface defects in transparent elements. *Sens. Actuators A Phys.* **2025**, *381*, 116049. [CrossRef]
38. Schröder, S.; Duparré, A.; Coriand, L.; Tünnermann, A.; Penalver, D.H.; Harvey, J.E. Modeling of light scattering in different regimes of surface roughness. *Opt. Express* **2011**, *19*, 9820–9835. [CrossRef]
39. Jähne, B. *Digitale Bildverarbeitung*, 8th ed.; Springer Vieweg: Wiesbaden, Germany, 2024.

Disclaimer/Publisher's Note: The statements, opinions and data contained in all publications are solely those of the individual author(s) and contributor(s) and not of MDPI and/or the editor(s). MDPI and/or the editor(s) disclaim responsibility for any injury to people or property resulting from any ideas, methods, instructions or products referred to in the content.